Soldati, Marco; Laakso, Ilkka

Computational errors of the induced electric field in voxelized and tetrahedral anatomical head models exposed to spatially uniform and localized magnetic fields

Published in:
Physics in Medicine and Biology

DOI:
10.1088/1361-6560/ab5dfb

Published: 10/01/2020

Document Version
Peer-reviewed accepted author manuscript, also known as Final accepted manuscript or Post-print

Please cite the original version:
Soldati, M., & Laakso, I. (2020). Computational errors of the induced electric field in voxelized and tetrahedral anatomical head models exposed to spatially uniform and localized magnetic fields. *Physics in Medicine and Biology*, *65*(1), Article 015001. https://doi.org/10.1088/1361-6560/ab5dfb

Computational errors of the induced electric field in voxelized and tetrahedral anatomical head models exposed to spatially uniform and localized magnetic fields

Marco Soldati[1], **Ilkka Laakso**[1,2]

E-mail: marco.soldati@aalto.fi
[1]Department of Electrical Engineering and Automation, Aalto University, Espoo, Finland
[2]Aalto Neuroimaging, Aalto University, Espoo, Finland

Abstract. At low and intermediate frequencies, the strength of the induced electric field is used as dosimetric quantity for human protection in the International Commission on Non-Ionizing Radiation Protection (ICNIRP) guidelines. To compute the induced electric field, numerical methods based on anatomically realistic voxel models are commonly used. However, grid-based models introduce staircase approximation errors when curved surfaces are discretized with voxels, particularly in correspondence of boundaries with large differences in electrical conductivity. By contrast, those kind of artefacts are absent in tetrahedral meshes. Here, we investigate the computational errors that affect voxelized and tetrahedral head models when exposed to uniform magnetic fields at 50 Hz, and localized exposure due to transcranial magnetic stimulation (TMS). Five subjects were considered, and for each of them four voxel grids and four tetrahedral meshes were reconstructed with different resolutions. The differences in the results were characterized by comparing the induced electric fields computed using those meshes/grids. The results showed modest discrepancies in the overall electric field distributions between the various grids and meshes. However, the peak electric field strengths were erroneous for both tetrahedral and voxel models. Therefore, post-processing techniques are needed to suppress those numerical artefacts. For this purpose, the 99.99th, or lower, percentile of the electric field strength was found to remove the numerical errors. In addition, we found that spatially averaging the electric fields over 2 mm cubical volumes, as described by the ICNIRP, was effective in removing most of the spuriously large electric fields. When spatial averaging was used, relative coarse head models consisting of approximately 1 mm voxels or tetrahedral meshes with 2 mm average side length were sufficient to mitigate the artefacts. Nonetheless, the additional percentile filtering might still be needed to suppress the erroneous values completely.

1. Introduction

In recent years, concerns about possible adverse health effects provoked by human exposure to electromagnetic fields have risen. International bodies have established basic restrictions for limiting electromagnetic field exposure. At low frequencies (1 Hz to 100 kHz), the induced electric field is used as dosimetric quantity for the basic restrictions in the International Commission on Non-Ionizing Radiation Protection (ICNIRP) guidelines (ICNIRP 2010) and the Institute of Electrical and Electronics Engineers (IEEE) standard (IEEE 2002). In the IEEE standard, homogeneous ellipses of different sizes are employed to model the body, and they are used to derive the basic restrictions for the induced electric fields. In the

ICNIRP guidelines, this relationship is obtained by referring to published data based on voxelized anatomical models. The main effect of the induced electric field on the neurons and neuronal networks is due to the perturbation of the membrane potential of those cells, leading to possible adverse transient nervous system responses. As a compromise between this electrophysiological phenomenon and computational constraints, ICNIRP states that the induced electric field should be averaged over a $2 \times 2 \times 2$ mm^3 volume (ICNIRP 2010).

The induced electric field can be determined with individualized computer simulations that use anatomical voxel models. However, cubic grids are inefficient in approximating curved boundaries. This staircase approximation error introduces numerical artefacts in the evaluation of the induced electric field (Caputa *et al* 2002, Laakso and Hirata 2012*b*, Dawson *et al* 1996, Dawson *et al* 2001), making the maximum value unreliable, especially at the interface of tissues with high electrical conductivity contrast. As a consequence, ICNIRP suggests removing those artefacts by calculating the 99th percentile value of the induced electric field for a specific tissue. The 99th percentile filtering was first suggested by Dawson *et al* (2001), who exposed homogeneous and layered spheres of different resolutions to uniform magnetic and electric fields. Large errors were identified when comparing the maximum values of the induced electric field obtained with numerical methods and analytical solutions, especially in the case of uniform electric exposure. Those errors depended on large conductivity contrast at the boundaries (i.e., air-skin interface), and they did not decrease with increased resolution. However, the 99th percentile represented a satisfactory estimate of the maximum field. Later on, the 99th percentile filtering was first used on whole-body voxelized models exposed to uniform electric (Hirata *et al* 2001) and magnetic (Dawson *et al* 2002) fields. The resolution of the anatomical models was in the order of 3 mm, resulting in poor segmentation. Both studies showed that discarding the largest 1% of induced electric values in different tissues (i.e., brain, spinal cord) produced a mitigation of the staircase approximation error. Later studies (Dimbylow 2005*a*, Li and Wu 2015, Santis *et al* 2015) applied the 99th percentile filtering to the skin for removing artefacts in the armpit and groin regions. However, several concerns about the 99th percentile filtering were also reported. For instance, the use of the 99th percentile was found to underestimate the peak induced electric field strength (De Santis *et al* 2013, Chen *et al* 2013), especially in the case of non-uniform exposure scenarios (Laakso and Hirata 2012*b*). On the other hand, numerical models based on tetrahedral volume meshes are unaffected by the staircase approximation errors. Therefore, they could be more suitable for modeling non-uniform exposure. Nonetheless, tetrahedral meshes may suffer from artefacts originated by low quality tetrahedra that have an adverse effect on the accuracy of numerical solutions (Nielsen *et al* 2018, Windhoff *et al* 2013).

The aim of this research was to investigate the computational errors that affect the induced electric field strengths in anatomically realistic voxelized and tetrahedral models of the head. Five healthy subjects were considered. For each of them, four tetrahedral meshes and four voxel-based models were generated from magnetic resonance (MR) images with different resolutions. The head models were exposed to spatially uniform magnetic field at 50 Hz along three different directions (anterior-posterior, top-to-bottom and lateral). At 50 Hz, the basic restrictions defined in the brain by the ICNIRP guidelines are based on preventing alterations of the activity of the synapses, which are considered as potentially sensitive sites for neural interaction with the induced electric field.

In addition, localized exposure produced by transcranial magnetic stimulation (TMS) was considered. TMS is a non-invasive technique enabling painless brain stimulation via a rapidly changing magnetic field generated by a coil fed with a strong pulse of electric current. The time-varying magnetic field produced by the coil, which is placed over the scalp, penetrates into the head inducing an electric field that interacts with neurons of the

brain. Although TMS is a medical application adopted for the treatment of neurological and psychiatric disorders (Ilmoniemi *et al* 1999), it offers the advantage to realistically simulate localized exposure due to intense magnetic fields.

This study represents the first investigation aimed at comparing the induced electric fields obtained in voxelized and tetrahedral anatomical models exposed to uniform and localized magnetic field. Herein, we used the finite-element method (FEM) to calculate the induced electric fields in each element of the generated meshes and grids. Since an analytical solution does not exist, we can only study the accuracy of the results based on the discrepancies among the computational methods. To characterize numerical uncertainties and discrepancies, the electric fields were computed and compared among anatomical models with different resolutions. Numerical errors in the evaluation of the maximum electric field values were observed in both voxel-based and tetrahedral models. Therefore, post-processing approaches based on percentile values as well as spatial averaging were considered to determine numerically robust ways to model both uniform and localized exposure of the central nervous system.

2. Materials and methods

2.1. Subjects and imaging methods

The subjects were five neurologically healthy male individuals aged 30 ± 4 years, who were enrolled in our previous study (Mikkonen and Laakso 2019). For each of them, high-resolution T1- and T2-weighted structural images were acquired using a 3 T scanner (Magnetom Skyra; Siemens, Ltd., Erlangen, Germany). The detailed settings used for the Magnetic Resonance Imaging (MRI) acquisitions are available in the prior investigation (Mikkonen and Laakso 2019).

2.2. Human models

The polygonal surfaces of the grey and white matter were reconstructed using FreeSurfer (Dale *et al* 1999), which is designed to work with T1-weighted images. A previously described semi-automatic procedure was implemented for the segmentation of non-brain tissues (Laakso *et al* 2015), which uses T2-weighted images for the reconstruction of tissues such as the scalp, skull, and the cerebrospinal fluid (CSF). For each subject, the final model was segmented in a grid of 0.5 mm cubic voxels to six compartments: skull, eyes, CSF, other tissues (e.g. scalp, muscle, nerves), grey matter (GM), and white matter (WM). The white matter of the cerebellum and the brainstem were treated as WM, whereas the grey matter of the cerebellum as GM. The segmented voxel model was then given as input for a 3D mesh generation toolbox (Fang and Boas 2009), namely *iso*2*mesh*, that allowed the creation of high quality tetrahedral meshes from 3D segmented images. For each subject, four tetrahedral head models were generated with different resolutions. The average edge lengths $\pm$ standard deviations (mm) among the subjects of those meshes are reported in Table 1, along with the average number of tetrahedral elements and nodes. Based on the mean edge lengths, the tetrahedral head models will be referred from now on as 2.14 mm, 1.60 mm, 1.31 mm, and 1.19 mm meshes. In addition, the quality of the head meshes were assessed by determining three metrics: ρ, η and γ (Liu and Joe 1994, Nielsen *et al* 2018, Zhang *et al* 2005). Metric ρ is defined as the ratio between the shortest and the longest edge of the tetrahedron; η, known as the Joe-Liu parameter, is proportional to the ratio between the tetrahedral volume and the sum of its edge lengths; and γ accounts for the relationship between the tetrahedral volume

and its total surface area. These metrics enable to assess whether an element is close to be a regular tetrahedron. Values of 1 represent the best quality, whereas 0 the worst quality. All the metrics were evaluated for each tetrahedron, and then averaged for each resolution of the meshes and across the subjects.

Table 1: Average edge lengths $\pm$ standard deviations (mm) across the five subjects of the meshes along with the average number of tetrahedral elements and nodes. Average time $\pm$ standard deviations (s) to assemble and solve the FEM system in the tetrahedral meshes. The CPU times were averaged across the subjects among the uniform and localized exposure scenarios.

	Mesh 1	Mesh 2	Mesh 3	Mesh 4
Edge length	2.14 ± 0.53	1.60 ± 0.30	1.31 ± 0.23	1.19 ± 0.20
Tetrahedra [$\times 10^6$]	4.49 ± 0.15	11.73 ± 0.44	21.34 ± 0.82	28.74 ± 1.10
Nodes [$\times 10^6$]	0.75 ± 0.02	1.93 ± 0.07	3.50 ± 0.13	4.70 ± 0.18
CPU time (uniform)	96.70 ± 5.85	306.03 ± 14.30	582.00 ± 31.06	850.51 ± 73.50
CPU time (TMS)	96.32 ± 5.57	312.05 ± 19.80	593.03 ± 37.85	860.02 ± 82.15

Once the finest tetrahedral meshes were obtained, they were used to create voxelized anatomical models with resolutions of 2 mm, 1 mm, 0.5 mm, and 0.25 mm. For this purpose, to each voxel of the new uniform grid, we assigned the same tissue type as the tetrahedron in which the center of the voxel was contained. This step ensured that the voxelized and tetrahedral models were as similar as possible after using *iso2mesh*. The average number of voxels and nodes in each grid are listed in Table 2. In Table 1 and Table 2, we also provide the CPU times needed to assemble and solve the FEM systems in terms of the elapsed real time ('wall time'), without including any preprocessing steps. The calculations were performed using a computer equipped with an Intel i7-7700K processor, 64 GB of memory, and running Ubuntu 18.04.2 LTS.

Table 2: Four voxel grid resolutions (mm) and the average ($\pm$ standard deviation) number of voxels and nodes across the five subjects. Average time $\pm$ standard deviations (s) to assemble and solve the FEM system in the voxel-based models. The CPU times were averaged across the subjects among the uniform and localized exposure scenarios.

	Grid 1	Grid 2	Grid 3	Grid 4
Edge length	2.0	1.0	0.5	0.25
Voxels [$\times 10^6$]	0.57 ± 0.02	4.55 ± 0.18	36.38 ± 1.42	291.14 ± 11.36
Nodes [$\times 10^6$]	0.6 ± 0.02	4.68 ± 0.17	36.88 ± 1.40	293.08 ± 11.38
CPU time (uniform)	0.90 ± 0.27	6.00 ± 1.35	36.50 ± 8.90	460.83 ± 50.22
CPU time (TMS)	1.45 ± 0.13	9.18 ± 1.01	67.61 ± 11.62	744.50 ± 85.60

2.3. Exposure scenarios

Four exposure conditions were investigated: three uniform and one localized. The head models were exposed to a spatially uniform magnetic field at 50 Hz directed along the *x*-, *y*-, and *z*-axis. The magnetic flux density was set to be equal to the reference level for general public exposure (0.2 mT) defined by the ICNIRP guidelines (ICNIRP 2010). In the case of localized exposure, a figure-of-eight coil was placed approximately over the C3 position of

the 10–20 EEG system with an anterior-posterior orientation, and tangentially to the skull. The distance between the coil and the skin was set to be 4 mm.

2.4. Tissue conductivities

The tissue conductivity values were assumed to be linear and isotropic and assigned to each tetrahedral or cubic element of the grids/meshes. For uniform exposure at 50 Hz, tissue conductivities were assigned based on the values determined by Dimbylow (Dimbylow 2005*a*): 0.1 S/m (other tissues), 0.045 S/m (skull), 1.5 S/m (eyes), 2.0 S/m (CSF), 0.1 S/m (grey matter), 0.06 S/m (white matter). For TMS, grey and white matter conductivity values were chosen according to previous studies (Soldati *et al* 2018, Laakso *et al* 2018): 0.215 S/m (grey matter) and 0.142 S/m (white matter). Skull conductivity (0.0215 S/m) was arbitrarily assigned as the average between the compact and spongy bone values (Akhtari *et al* 2002), and increased by 30% to compensate for room temperature measurements. For the remaining tissues, the conductivity values were: other tissues, 0.43 S/m (Wake *et al* 2016); CSF, 1.79 S/m (Baumann *et al* 1997); eyes, 1.6 S/m (Lindenblatt and Silny 2001).

2.5. Electric field modeling

The electric field calculations were performed under the quasi-static assumption (Wang and Eisenberg 1994), that allows to express the electric scalar potential ϕ as:

$$\nabla \cdot \sigma \nabla \phi = \nabla \cdot \sigma \frac{\partial}{\partial t} \mathbf{A}, \tag{1}$$

where σ is the electrical conductivity of tissue and $\mathbf{A}$ is the magnetic vector potential. The time derivative in the magnetic vector potential $\mathbf{A}$ is analytically calculated and then used as input for the FEM analysis to determine the electric scalar potential ϕ. In the case of the spatially uniform exposure, the magnetic vector potential $\mathbf{A}$ was given by a strong point-wise magnetic dipole placed very far away from the head, and oriented in three orthogonal directions: antero-posterior (AP), top-to-bottom (TOP) and lateral (LAT). For TMS, the magnetic vector potential was determined by modeling the coil, namely the standard Magstim 70 mm coil (P/N 9790), as a series of magnetic dipoles (Thielscher and Kammer 2004, Thielscher and Kammer 2002). Therefore, the total vector potential $\mathbf{A}$ was given as the summation of contributions from all the dipoles. All the simulations were performed using a rate of change of the coil current of 10^6 A/s. Once determined the magnetic vector potential $\mathbf{A}$, the induced electric field is calculated from the gradient of the scalar potential by making use of the following equation:

$$\mathbf{E} = -\nabla \phi + \frac{\partial}{\partial t} \mathbf{A}, \tag{2}$$

In this study, two different solvers were used to compute the electric fields in the voxelixed and tedrahedral anatomical models. For the meshes, we employed SimNIBS (Thielscher *et al* 2011, Windhoff *et al* 2013, Saturnino *et al* 2018) to solve the electric scalar potential from (1), whose version 2.1 uses the open-source FEM software GetDP (Geuzaine 2007, Saturnino *et al* 2019). In particular, GetDP is based on the conjugate gradient (CG) method and the incomplete Cholesky preconditioner. Manuals and tutorials are available online (*http://simnibs.de*). For the voxel models, the equation (1) was solved through our in-house finite element solver (Laakso and Hirata 2012*a*), which uses the geometric multigrid method with successive over-relaxation. In both computational approaches, piece-wise linear basis functions were used. The spatial discretization for the grid models was set to be 2 mm,

1 mm, 0.5 mm, and 0.25 mm, corresponding to the side length of the cubic cells applied for the volume conductor models. The weights and positions of the dipoles were verified to be exactly equal to the ones used in SimNIBS to generate the uniform and localized exposures. The residual norm was set to be lower than 10^{-10} in all the simulations for both computational approaches.

Each of the computational techniques was validated by comparing the numerical results with the analytical solution in a sphere exposed to uniform magnetic field at 50 Hz directed along the *x*-axis. The detailed analysis and results are available in the Supplementary material 3.

2.6. Discrepancies in the computed electric fields

For both tetrahedral and voxelized head models, the electric field was interpolated on a surface at the middle between the surfaces of the grey and white matter, to avoid evaluating the field on the boundary of tissues having different conductivities. On this surface, the discrepancies in the results were evaluated by calculating the relative difference defined as follows:

$$\texttt{relative difference} = \frac{\sqrt{\sum_{n\in S} |\mathbf{E}_n^i - \mathbf{E}_n^0|^2}}{\sqrt{\sum_{n\in S} |\mathbf{E}_n^0|^2}}, \tag{3}$$

where S is the set of all the elements contained in the middle surface between WM and GM, $\mathbf{E}_n^i$ the electric field in the node n for the tetrahedral or voxelized model i, and $\mathbf{E}_n^0$ the reference solution. The reference solution was the electric field determined in the finest voxel model of 0.25 mm resolution. We also calculated the differences among the electric field magnitudes by replacing $\mathbf{E}_n^i$ and $\mathbf{E}_n^0$ with $\left|\mathbf{E}_n^i\right|$ and $\left|\mathbf{E}_n^0\right|$, respectively.

2.7. Electric field averaging and percentiles

To account for neuronal activation, ICNIRP recommends determining the vector average of the induced electric field over a contiguous tissue volume of $2\times2\times2$ mm^3. To remove numerical artefacts, the 99th percentile value in a specific tissue needs to be considered as the relevant quantity when comparing it with the basic restriction (ICNIRP 2010). In this study, four tetrahedral and four voxel models were reconstructed for each subject, and the electric field was calculated at each element of the meshes/grids for uniform and localized exposures (TMS). In order to perform the average over a volume of $2\times2\times2$ mm^3, the electric field calculated in the tetrahedral meshes was interpolated over a cubic grid with a resolution of $2/7$ mm. This approach allowed performing a moving average by using a convolution kernel 3D-matrix consisting of an odd number of elements ($7\times7\times7$), with one voxel representing the center point of the averaging volume. Each element of the convolution kernel was equal to 1 divided by the total number of elements in the filter. Therefore, the moving average simply took the mean of the voxels in the kernel. In the case of the cubic resolution of 2 mm, the ICNIRP-averaged electric field in each voxel corresponds to the electric field value at the center point of the voxel. For the remaining 1 mm, 0.5 mm, and 0.25 mm grids, the same averaging approach used for the tetrahedral meshes was employed. In compliance with the ICNIRP recommendations (ICNIRP 2010), the average was performed exclusively for the voxels whose averaging volume was completely within the tissue of interest, without extending beyond the boundary of the tissues. Once the electric field was averaged, the 99th, 99.9th, and 99.99th percentiles and the maximum value were calculated for four different compartments (GM, WM, skull, and other tissues) and then averaged across the subjects.

Subsequently, the determined percentiles were compared with the ones extracted for the non-averaged electric fields.

3. Results

3.1. Human models

Figure 1 (a-g) represents the reconstructed tetrahedral head model of a representative subject consisting of six compartments. The metrics ρ, η, and γ were computed for each tetrahedron, and then averaged across the meshes and among the different subjects. Table 3 provides the average statistics, which includes the mean and the minimum values of the averaged parameters along with the averaged percentage of tetrahedra that exhibited values less than 0.1. This threshold represents the minimum quantity for acceptable well-shaped tetrahedra (Nielsen *et al* 2018).

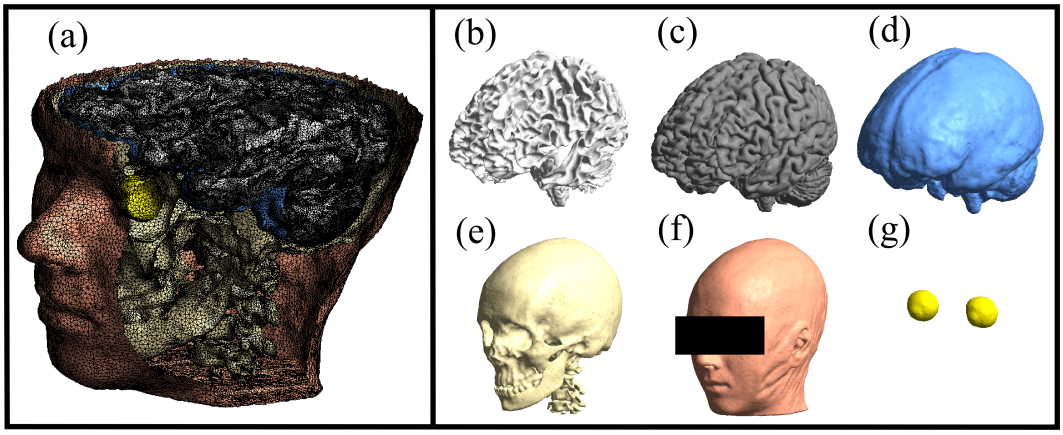

Figure 1: (a) Tetrahedral head model showing the reconstructed surface of the six compartments: (b) white matter, (c) grey matter, (d) CSF, (e) bone, (f) other tissues, and (g) eyes.

Table 3: Summary of the average statistics of the metrics ρ, η and γ. The values represent the mean and standard deviation of the metrics averaged across the different resolutions of the meshes and among the subjects. The columns list the minimum values, percentage of low-quality tetrahedra, and the mean values.

Mesh	ρ			η		
	min (std)	% < 0.1 (std)	mean (std)	min (std)	% < 0.1 (std)	min (std)
2.14 mm	0.158 (0.0027)	0.0	0.529 (0.0018)	0.075 (0.017)	9.7e-05 (2.4e-05)	0.704 (0.0021)
1.60 mm	0.168 (0.0019)	0.0	0.623 (0.0008)	0.113 (0.018)	1.7e-06 (3.8e-06)	0.804 (0.008)
1.31 mm	0.167 (0.0060)	0.0	0.643 (0.0006)	0.124 (0.022)	1.0e-06 (2.2e-06)	0.822 (0.005)
1.19 mm	0.165 (0.0033)	0.0	0.648 (0.0005)	0.123 (0.016)	6.8e-07 (1.5e-06)	0.826 (0.005)
Mesh	γ					
	min(std)	% < 0.1 (std)	mean(std)			
2.14 mm	0.026 (0.0096)	4.7e-02 (2.0e-03)	0.570 (0.0025)			
1.60 mm	0.042 (0.0108)	3.5e-03 (6.7e-05)	0.662 (0.0017)			
1.31 mm	0.049 (0.0056)	9.9e-04 (6.7e-05)	0.678 (0.0011)			
1.19 mm	0.049 (0.0062)	6.2e-04 (5.5e-05)	0.682 (0.0009)			

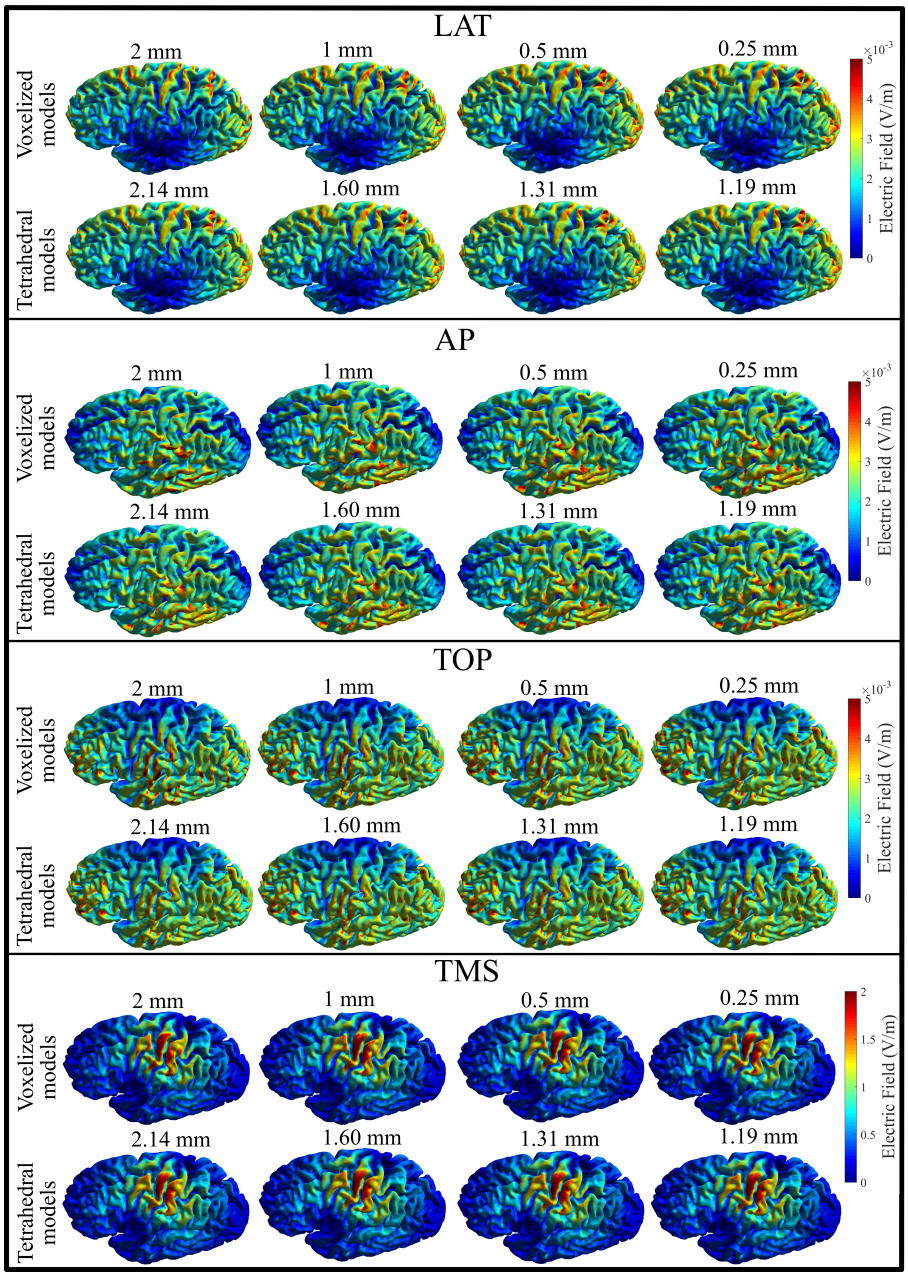

Figure 2: Induced electric fields in the left hemisphere shown on a surface in the middle between the surfaces of the grey and white matter for a representative head model. The electric field distributions were obtained for uniform exposure to 0.2 mT magnetic flux density at 50 Hz (LAT, AP, and TOP directions). In TMS, the results show the induced electric field calculated using a rate of change of the coil current of 10^6 A/s.

3.2. Electric field distributions and discrepancies

Figure 2 shows the magnitude of the electric field for a representative head model induced by uniform magnetic field (0.2 mT) exposure at 50 Hz for the TOP, AP, and LAT directions,

and the results in the case of the locally applied magnetic field generated by TMS. The induced electric fields were computed using both voxel grids and tetrahedral meshes and then interpolated on a surface situated in the middle between the surfaces of the white and grey matter for visualization. By visual inspection, all meshes and grids produce similar electric field distributions, indicating that all of them are sufficient for producing physically appropriate results.

To quantify the discrepancies in the results, we calculated the average relative difference across the subjects for each mesh/grid (Figure 3). The relative difference was calculated with respect to the reference solution of the 0.25 mm voxel-based head model. As shown, there was a good accordance in terms of induced electric field evaluated in the voxelized and tetrahedral models, and the discrepancies decreased as the meshes/grids became finer. The mean relative difference became smaller in the case of localized exposure due to TMS.

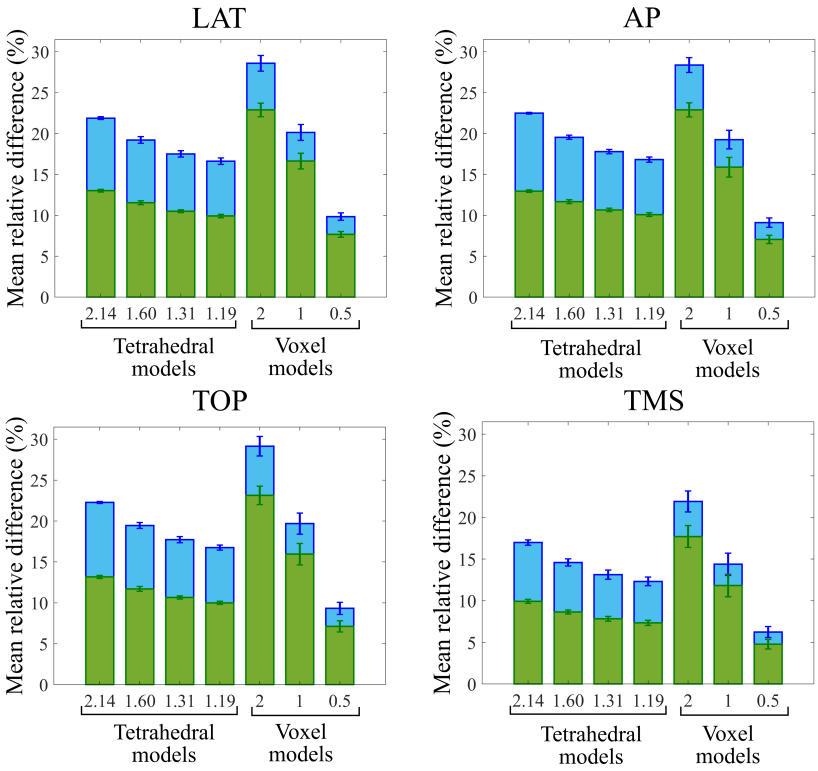

Figure 3: Mean relative difference of tetrahedral and voxel models calculated in relation to the results obtained for the 0.25 mm cubic grid. The values on the horizontal axis are the different mesh/grid resolutions of the head models. For each exposure scenario, the blue bars indicate the relative difference which includes the three vector components of the electric field, whereas the green bars quantify the relative difference in the magnitude of the electric field.

3.3. Computed percentiles

For each subject and for each mesh/grid, the electric field strengths were extracted from four different compartments and arranged in ascending order to calculate the 99th, 99.9th, and

99.99th percentiles along with the maximum electric field strengths. The percentiles were calculated as the electric field value exceeded in 1%, 0.1%, and 0.01% of the volume in each tissue compartment, respectively. Figure 4 shows the results averaged across the subjects for the different resolutions of the mesh/grid in each exposure scenario. The data derived for each individual is available in Supplementary material 1. The individual data were similar to the averaged data, and thus, in the following we only discuss the data averaged across the subjects.

A good agreement between the meshes/grids in the computed values is observed up to the 99.99th percentile, after which they diverge with a rapid increase in the electric field strength until reaching the maximum value. This trend is observed in all tissue compartments. Considering the uniform exposure scenarios, the lateral orientation is found to produce the highest electric field strength since the brain exhibits the largest cross-section in the sagittal plane. Among the voxel grids, the highest electric field value decreases from the finest to the coarsest resolution. Those erroneous and large electric fields are caused by the staircase approximation errors, i.e., the discretization of curved surfaces with voxels, that make the maximum electric field value unreliable especially at the boundaries with high electrical conductivity contrast. Even in the case of the tetrahedral models, the maximum electric field strengths differ greatly between the different meshes, indicating that the maximum values are affected by numerical artefacts. These are mainly caused by low quality tetrahedra, which will be shown in the following.

In order to check which elements are affected by high electric fields, Figure 5 provides a comprehensive volumetric map of the voxels and tetrahedra whose induced electric field is higher than the 99th percentile. The results are derived from both localized and uniform exposure in the LAT direction for a representative subject. The maximum value of the electric field is highlighted with cerulean colored circles. To avoid repetition, we only show the coarsest and finest meshes/grids, given that similar outcomes are observed for the other resolutions. As clearly shown, in the uniform exposure scenario, the electric field is more intense in proximity of thin tissues at the boundary with regions characterized by large conductivity contrasts (i.e., air/skin interface). Overall, both computational models provide an analogous volumetric distribution of voxels and tetrahedra with the high electric field strength. However, the grid-based models result in several voxels with spuriously electric field strengths at tissue boundaries. These hotspots are due to the staircasing errors and are absent in the tetrahedral meshes, where the electric field distributions appear to be smoother. Despite the latter not being affected by this artefact, they rely on the geometrical quality of the meshes. In particular, the maximum electric field value is susceptible to low quality elements. In this regard, we calculated the metrics ρ, η and γ of the tetrahedron that exhibits the maximum electric field for each tissue compartment, and averaged them across the meshes and among the subjects. Results are given in Figure 6, which shows all the metrics to be smaller than those reported in Table 3. In particular, the parameter γ drops to values around 0.2. This means the highest electric fields are found in poorer-quality tetrahedra, making the maximum electric field unreliable. The parameter γ improves in the GM and WM in the case of TMS, meaning that the effect of low quality tetrahedra on the high electric field values reduces in the areas underlying the localized exposure, as revealed in Figure 6 (d). As a consequence, the location of the maximum electric field remains delimited in the WM and GM over a small region under the stimulation coil, whereas it is more widespread for uniform exposures.

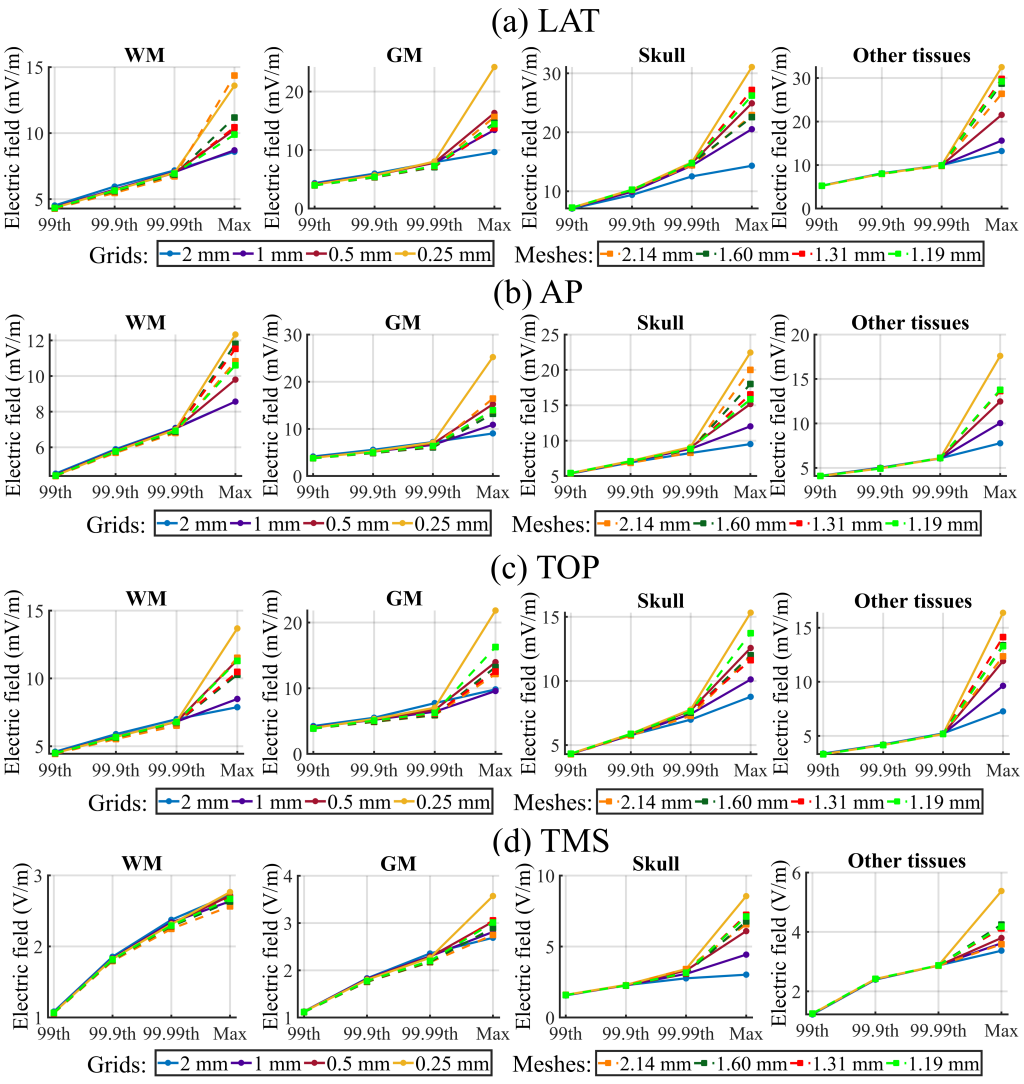

Figure 4: The 99th, 99.9th, and 99.99th percentiles along with the maximum electric field strength extracted from four tissue compartments. Data is averaged across the subjects for each mesh/grid resolution. (a-c) Uniform exposure along LAT, AP and TOP directions to 0.2 mT magnetic flux density at 50 Hz. (d) Localized exposure due to TMS.

3.4. Percentiles derived from averaging over $2 \times 2 \times 2$ mm^3 *cube*

The electric field was averaged over a contiguous tissue volume of $2 \times 2 \times 2$ mm^3, except for the grid-based models of 2 mm resolution where the values in each element correspond to the electric field at the center point of the voxel. As done previously, the 99th, 99.9th, and 99.99th percentiles along with the maximum electric field values were subsequently extracted for each tissue of the head models and then averaged across the subjects (Figure 7). The data derived for each subject is available in Supplementary material 2.

For the uniform magnetic exposure at the general public reference level of 0.2 mT

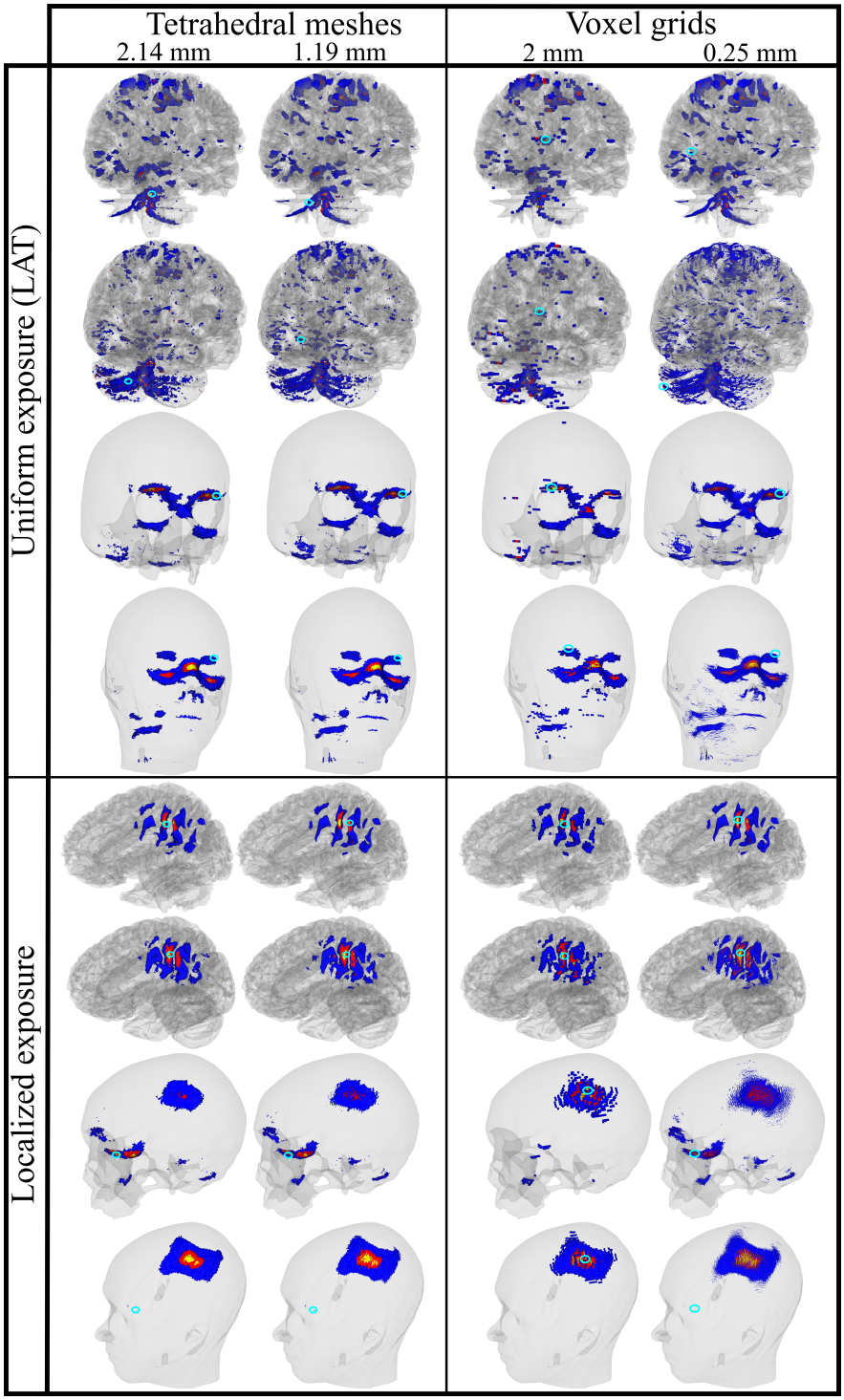

Figure 5: Volumetric maps of the tissue compartments showing the voxels and tetrahedra in correspondence of which the magnitude of the induced electric field is higher than the 99th percentile. Localized and uniform exposure in LAT direction for a representative subject. Blue elements represent electric fields between the 99th and 99.9th percentile, the red ones range from the 99.9th to the 99.99th percentile, and the yellows exhibit values higher than the 99.99th percentile. Maximum value of the electric field highlighted with cerulean colored circles.

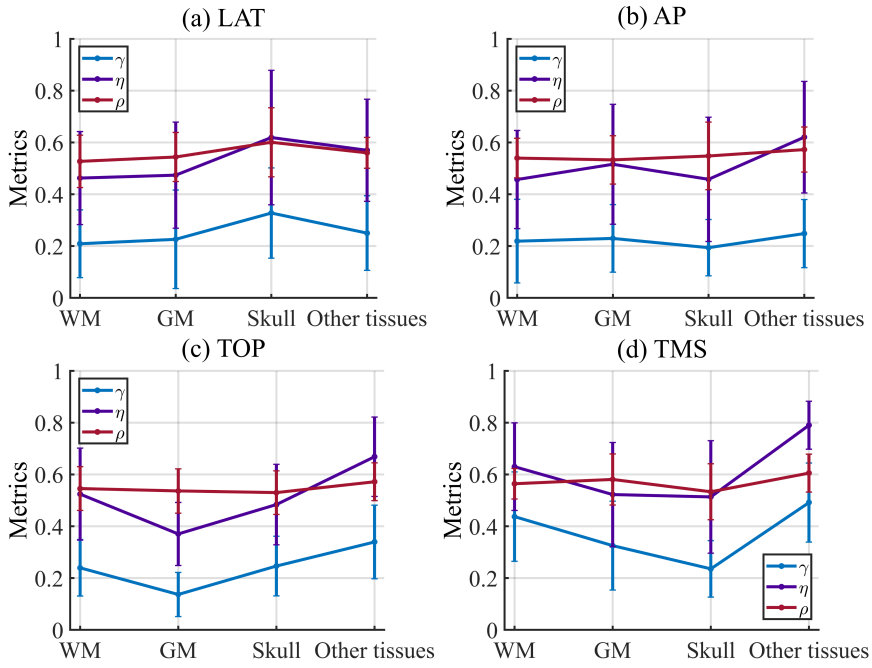

Figure 6: Metrics ρ, η and γ calculated for the tetrahedra corresponding to the maximum electric field in each tissue compartment. Data is averaged across the different resolution of the meshes and among the subjects. (a-c) Uniform exposure along LAT, AP and TOP directions to 0.2 mT magnetic flux density at 50 Hz. (d) Localized exposure due to TMS.

(ICNIRP 2010), the peak ICNIRP-averaged electric fields and the respective 99th percentiles were always in compliance with the basic restriction limit of 20 mV/m. When comparing with the non-averaged electric fields (Figure 4), averaging over the $2 \times 2 \times 2$ mm^3 cube mitigates the erroneous high electric field values due to numerical errors. In particular, the changes in the maximum electric field values are large compared to the changes in the 99th, 99.9th, and 99.99th percentiles.

4. Discussion

This work represents the first attempt to compare the induced electric fields computed in voxelized and tetrahedral head models when exposed to uniform magnetic fields at 50 Hz. The computational errors affecting those models were also characterized. So far, prior investigations examined mainly grid-based models (Dimbylow 2005*a*, Chen *et al* 2013, Santis and Chen 2014, Bakker *et al* 2012, Hirata *et al* 2011). Additional novelties are represented by the study of the effect of localized magnetic field exposure on the artefacts, and the evaluation of the 99th, 99.9th, 99.99th percentiles along with the maximum electric fields for different tissues, rather than considering the whole head as a single compartment. Two different solvers were used to compute the induced electric fields: a freely available open source software package (SimNIBS) and our in-house solver, which are both based on FEM. The former uses tetrahedral meshes whereas the latter employs voxel-based models.

In the anatomical head models, both computational approaches produced overall similar

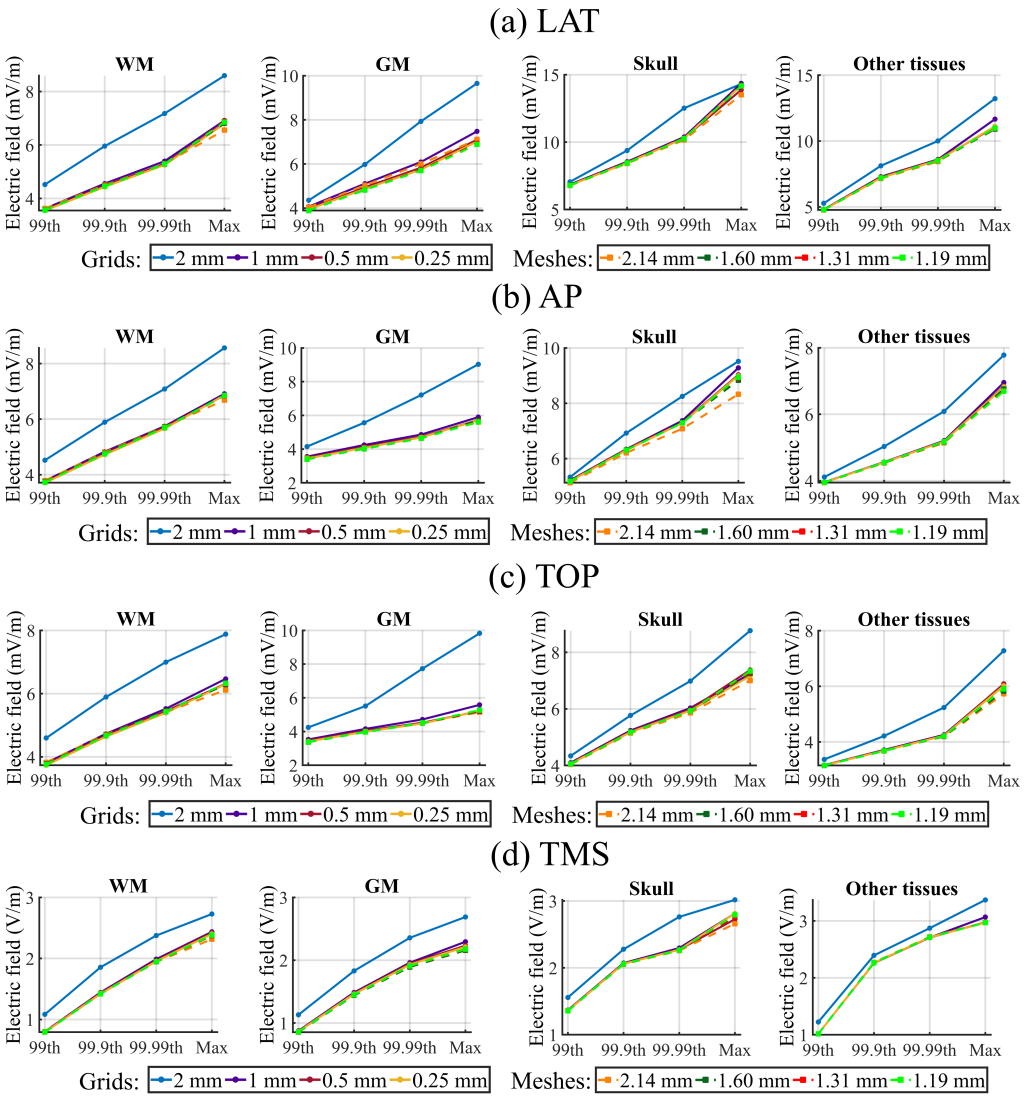

Figure 7: The 99th, 99.9th, and 99.99th percentiles along with the maximum electric field strength extracted after averaging the electric field over $2 \times 2 \times 2$ mm^3 cube. Results are averaged across the subjects for each resolution of the mesh/grid. (a-c) Uniform exposure along LAT, AP and TOP directions to 0.2 mT magnetic flux density at 50 Hz. (d) Localized exposure due to TMS.

electric field distributions. Calculating the actual error in the results is not possible due to the lack of an analytical solution. As a consequence, to assess the discrepancies between the induced electric fields obtained in the voxel-based and tetrahedral models, the finest grids were considered as a reference since containing the largest number of elements. However, those are hardly deprived from artefacts. The discrepancies among the meshes/grids, computed in terms of relative difference with respect to our finest solution, decreased as the resolution became finer, suggesting that the results converged towards the same solution. This assessment

provides a global estimate of the discrepancies between the computational methods, since the relative difference does not consider potentially large local differences.

Both voxelized and tetrahedral head models suffered from artefacts in the evaluation of the high electric field values. In the grid-based models, those numerical errors were caused by the staircase approximation errors (Laakso and Hirata 2012*b*), that originate when curved boundaries are approximated with voxels. The staircasing error depends on the resolution of the grid and on large conductivity contrasts between curved boundaries. The finer the resolution, the higher the value of the maximum electric field. Even though tetrahedral meshes are not affected by staircase approximation errors, they rely on the geometrical quality of the tetrahedra. Despite having no effect on the overall electric field distribution, poorly-shaped elements produce artefacts that make the maximum electric field unreliable. Generating meshes consisting for the totality of equilateral tetrahedra is rather challenging. Here, we assessed the quality of tetrahedral head models by calculating commonly used metrics, which were found to be comparable with high quality meshes present in the literature (Nielsen *et al* 2018, Windhoff *et al* 2013). Even though the percentage of low-quality tetrahedra was negligible compared to the total number of elements, those affected the accuracy of the FEM results in the evaluation of the maximum electric field.

The averaging over a contiguous tissue volume of $2 \times 2 \times 2$ mm^3 has been introduced by the ICNIRP guidelines (ICNIRP 2010) to consider the effect of the induced electric field on the excitable cells (i.e., neurons and nerves). However, this spatial averaging was also found to be effective in removing most of the numerical artefacts in both tetrahedral meshes/voxel grids. Overall, voxel grids of approximately 1 mm resolution and meshes consisting of tetrahedra with average side length of 2 mm were sufficient to mitigate the artefacts when the averaging over a $2 \times 2 \times 2$ mm^3 cube was performed. Therefore, there is no need to implement extremely fine grids/meshes, which can lead to considerable advantages in terms of computational costs. This applies also to the non-averaged electric field strengths when at least the 99.99th percentile filtering is used. Based on the ICNIRP-averaged data obtained for each individual (Supplementary material 2), the peak values still showed a slight dispersion in the results, indicating that additional percentile filtering might be needed to suppress the artefacts completely. For this purpose, the use of the 99th percentile, as recommended in the ICNIRP guidelines, was proved to be effective in each exposure scenario for all the mesh/grid resolutions. Moreover, we found that using higher percentile values, 99.9th or 99.99th, was already sufficient for removing the artefacts in both the averaged and non-averaged electric field strengths.

By definition, 99th percentile filtering produces underestimation of the maximum induced electric field strength. In the case of the 0.25 mm head models exposed to homogeneous magnetic fields, the 99th percentile filtering of the spatially averaged electric fields was on average 45% lower than the corresponding peak values in WM, 40% in GM, 45% in the skull, and 48% in the other tissues. The peak spatially averaged electric fields and corresponding 99th percentiles were found to be always in compliance with the ICNIRP (ICNIRP 2010) basic restriction for reference level exposure at 50 Hz. Even the maximum spatially averaged values were less than a third of the basic restriction, indicating a certain margin of conservatism in the reference levels. For localized exposure, this difference becomes more significant: the 99th percentile filtering was on average 65% lower than the peak values in the WM, 60% in the GM, 50% in the skull, and 65% in the other tissues. These results are consistent with previous studies showing that the 99th percentile filtering of non-averaged electric fields causes notable underestimation of the exposure. For example, Chen *et al* (2013) estimated the 99th percentile to be approximately 50% below the maximum spatially averaged values derived for the whole brain exposed to LAT uniform magnetic field at 50 Hz.

For locally applied magnetic fields, Laakso and Hirata determined an underestimation of 40% of the maximum electric field value due to the 99th percentile filtering using a layered sphere (Laakso and Hirata 2012*b*).

This study has some limitations. First of all, the anatomical volume conductor models generated in this investigation represent simplified head models of six compartments, whereas in reality the head is a more complex structure consisting of many other tissues. For example, the compartment 'other tissue' included scalp, subdural fat, muscle and nerves, making the assignment of a single conductivity to this tissue complicated. More accurate head models could lead to a better estimation of the induced electric fields in different tissues. Differences in segmentation should also be considered when comparing our results to literature values; in a previous study (Dimbylow 2005*b*), the 99th percentile electric field strengths are slightly higher than those presented herein, since they were derived for the whole brain rather than for individual GM and WM compartments. In addition, TMS was considered as an example of localized exposure. In the simulations performed herein, the coil was placed over a region where the skin was relatively smooth. However, the stimulation in the vicinity of regions where the induced current changes sharply in direction (i.e., the pinna) could make the electric field more sensitive to the staircase approximation error. Lastly, the anatomical volume conductors were cut at the level of the neck. Therefore, the results derived here cannot be generalized for the tissues extending below the head (bone and other tissues), especially in uniform exposure scenarios. This assumes particular significance if considering that the 99th percentile filtering was introduced as a metric for the whole body to remove numerical errors in regions of the skin such as the armpits and groins (Li and Wu 2015, Santis *et al* 2015, Reilly and Hirata 2016). As the results of the truncation of the anatomical models, this investigation is exempt from such artefacts, which are originated by the sharp change in direction of the induced current that causes intense electric fields also in underlying tissues. However, in the case of localized exposure, the significance of the percentiles depends on the relative volume of the exposed area. For example, assuming that only 10% of the total volume is exposed, then the 99.9th percentile calculated over the entire volume would be the same as the 99.9th percentile in the exposed region. This effect has been partially discussed in a recent investigation (Gomez-Tames *et al* 2018) for non-uniform exposure.

5. Conclusion

In this research, similar electric field distributions were obtained using voxelized and tetrahedral head models exposed to localized and uniform magnetic fields. The discrepancies in the computed values, calculated with respect to the results obtained in the finest grids, reduced as the resolution increased. However, both models were affected by computational errors in the evaluation of the highest electric fields. Those numerical artefacts were due to the staircase approximation error in the grid-based models, and mainly low-quality tetrahedra in the meshes. The averaging over a contiguous tissue volume over a $2 \times 2 \times 2$ mm^3 volume was effective in removing most of the artefacts in both voxelized and tetrahedral head models, indicating that the additional percentile filtering is still needed to suppress them completely. Also the use of the 99.99th, or lower, percentile of non-averaged electric fields allowed to mitigate the computational errors in the exposure assessment of the tissues of the central nervous system. The results aid the development of numerically robust dosimetric quantities for both human exposure guidelines and computational exposure assessment protocols.

Acknowledgement

The authors would like to thank Prof. Akimasa Hirata (Department of Computer Science and Engineering, Nagoya Institute of Technology, Nagoya, Japan) for his valuable support and useful discussions on the topics of this research.

References

Akhtari M, Bryant H C, Mamelak A N, Flynn E R, Heller L, Shih J J, Mandelkern M, Matlachov A, Ranken D M, Best E D, DiMauro M A, Lee R R and Sutherling W W 2002 Conductivities of three-layer live human skull *Brain Topogr* **14**(3) 151–67

Bakker J F, Paulides M M, Neufeld E, Christ A, Chen X L, Kuster N and van Rhoon G C 2012 Children and adults exposed to low-frequency magnetic fields at the ICNIRP reference levels: theoretical assessment of the induced electric fields *Phys Med Biol* **57**(7) 1815–29

Baumann S, Wozny D, Kelly S and Meno F 1997 The electrical conductivity of human cerebrospinal fluid at body temperature *IEEE Trans Biomed Eng* **44**(3) 220–3

Caputa K, Dimbylow P J, Dawson T W and Stuchly M A 2002 Modelling fields induced in humans by 50/60 Hz magnetic fields: reliability of the results and effects of model variations *Phys Med Biol* **47**(8) 1391–8

Chen X L, Benkler S, Chavannes N, De Santis V, Bakker J, van Rhoon G, Mosig J and Kuster N 2013 Analysis of human brain exposure to low-frequency magnetic fields: A numerical assessment of spatially averaged electric fields and exposure limits *Bioelectromagnetics* **34**(5) 375–384

Dale A M, Fischl B and Sereno M I 1999 Cortical surface-based analysis. i. segmentation and surface reconstruction *Neuroimage* **9**(2) 179–94

Dawson T W, Caputa K and Stuchly M A 2002 Electric fields induced in humans and rodents by 60 Hz magnetic fields *Phys Med Biol* **47**(14) 2561–8

Dawson T W, Moerloose J D and Stuchly M A 1996 Comparison of magnetically induced ELF fields in humans computed by FDTD and scalar potential FD codes *Appl. Comput. Elecromagn. Soc. J.* **11**(3) 63–71

Dawson T W, Potter M and Stuchly M A 2001 Evaluation of modeling accuracy of power frequency field interactions with the human body *Appl. Comput. Elecromagn. Soc. J.* **16**(2) 162–72

De Santis V, Chen X L, Laakso I and Hirata A 2013 On the issues related to compliance of LF pulsed exposures with safety standards and guidelines *Phys Med Biol* **58**(24) 8597–607

Dimbylow P 2005*a* Development of the female voxel phantom, NAOMI, and its application to calculations of induced current densities and electric fields from applied low frequency magnetic and electric fields *Phys Med Biol* **50**(6) 1047–70

Dimbylow P 2005*b* Resonance behaviour of whole-body averaged specific energy absorption rate (SAR) in the female voxel model, NAOMI *Phys Med Biol* **50**(17) 4053–63

Fang Q and Boas D A 2009 Tetrahedral mesh generation from volumetric binary and grayscale images.*in* '2009 IEEE International Symposium on Biomedical Imaging: From Nano to Macro'pp. 1142–1145

Geuzaine C 2007 GetDP: a general finite-element solver for the de rham complex *PAMM* **7**(1) 1010603–1010604

Gomez-Tames J, Laakso I, Haba Y, Hirata A, Poljak D and Yamazaki K 2018 Computational artifacts of the in situ electric field in anatomical models exposed to low-frequency magnetic field *IEEE Transactions on Electromagnetic Compatibility* **60**(3) 589–597

Hirata A, Caputa K, Dawson T W and Stuchly M A 2001 Dosimetry in models of child and adult for low-frequency electric field *IEEE Transactions on Biomedical Engineering* **48**(9) 1007–1012

Hirata A, Takano Y, Fujiwara O, Dovan T and Kavet R 2011 An electric field induced in the retina and brain at threshold magnetic flux density causing magnetophosphenes *Phys Med Biol* **56**(13) 4091–101

ICNIRP 2010 Guidelines for limiting exposure to time-varying electric and magnetic fields (1 Hz to 100 kHz) *Health Phys* **99**(6) 818–36

IEEE 2002 IEEE Standard for Safety Levels with Respect to Human Exposure to Electromagnetic Fields, 0-3 kHz, C95.6-2002 (New York: Institute of Electrical and Electronics Engineers)

Ilmoniemi R J, Ruohonen J and Karhu J 1999 Transcranial magnetic stimulation–a new tool for functional imaging of the brain *Crit Rev Biomed Eng* **27** 241–284

Laakso I and Hirata A 2012*a* Fast multigrid-based computation of the induced electric field for transcranial magnetic stimulation *Phys Med Biol* **57**(23) 7753–65

Laakso I and Hirata A 2012*b* Reducing the staircasing error in computational dosimetry of low-frequency electromagnetic fields *Phys Med Biol* **57**(4) N25–34

Laakso I, Murakami T, Hirata A and Ugawa Y 2018 Where and what TMS activates: experiments and modeling *Brain Stimul* **11** 166–174

Laakso I, Tanaka S, Koyama S, De Santis V and Hirata A 2015 Inter-subject variability in electric fields of motor cortical tDCS *Brain Stimul* **8**(5) 906–13

Li C and Wu T 2015 Dosimetry of infant exposure to power-frequency magnetic fields: Variation of 99th percentile induced electric field value by posture and skin-to-skin contact *Bioelectromagnetics* **36**(3) 204–218

Lindenblatt G and Silny J 2001 A model of the electrical volume conductor in the region of the eye in the ELF range *Phys Med Biol* **46**(11) 3051–59

Liu A and Joe B 1994 Relationship between tetrahedron shape measures *BIT Numerical Mathematics* **34**(2) 268–287

Mikkonen M and Laakso I 2019 Effects of posture on electric fields of non-invasive brain stimulation *Physics in Medicine & Biology* **64**(6) 065019

Nielsen J D, Madsen K H, Puonti O, Siebner H R, Bauer C, Madsen C G, Saturnino G B and Thielscher A 2018 Automatic skull segmentation from mr images for realistic volume conductor models of the head: Assessment of the state-of-the-art *NeuroImage* **174** 587 – 598

Reilly J P and Hirata A 2016 Low-frequency electrical dosimetry: research agenda of the ieee international committee on electromagnetic safety *Physics in Medicine and Biology* **61**(12) R138

Santis V D and Chen X L 2014 On the issues related to compliance assessment of ICNIRP 2010 basic restrictions *Journal of Radiological Protection* **34**(2) N31–N39

Santis V D, Chen X L, Laakso I and Hirata A 2015 An equivalent skin conductivity model for low-frequency magnetic field dosimetry *Biomedical Physics & Engineering Express* **1**(1) 015201

Saturnino G B, Madsen K H and Thielscher A 2019 Efficient electric field simulations for transcranial brain stimulation *bioRxiv*

Saturnino G B, Puonti O, Nielsen J D, Antonenko D, Madsen K H and Thielscher A 2018 Simnibs 2.1: A comprehensive pipeline for individualized electric field modelling for transcranial brain stimulation *bioRxiv*

Soldati M, Mikkonen M, Laakso I, Murakami T, Ugawa Y and Hirata A 2018 A multi-scale computational approach based on TMS experiments for the assessment of electro-stimulation thresholds of the brain at intermediate frequencies *Physics in Medicine & Biology* **63**(22) 225006–

Thielscher A and Kammer T 2002 Linking physics with physiology in TMS: A sphere field model to determine the cortical stimulation site in TMS *Neuroimage* **17**(3) 1117–30

Thielscher A and Kammer T 2004 Electric field properties of two commercial figure-8 coils in TMS: calculation of focality and efficiency *Clin Neurophysiol* **115**(7) 1697–708

Thielscher A, Opitz A and Windhoff M 2011 Impact of the gyral geometry on the electric field induced by transcranial magnetic stimulation *Neuroimage* **54**(1) 234–43

Wake K, Sasaki K and Watanabe S 2016 Conductivities of epidermis, dermis, and subcutaneous tissue at intermediate frequencies *Phys Med Biol* **61**(12) 4376

Wang W and Eisenberg S 1994 A three-dimensional finite element method for computing magnetically induced currents in tissues *IEEE T Magn* **30**(6) 5015–23

Windhoff M, Opitz A and Thielscher A 2013 Electric field calculations in brain stimulation based on finite elements: An optimized processing pipeline for the generation and usage of accurate individual head models *Hum Brain Mapp* **34**(4) 923–35

Zhang Y, Bajaj C and Sohn B S 2005 3d finite element meshing from imaging data *Computer Methods in Applied Mechanics and Engineering* **194**(48) 5083 – 5106